
Splat-SLAM: Globally Optimized RGB-only SLAM with 3D Gaussians

Erik Sandström*
Google
ETH Zürich

Keisuke Tateno
Google

Michael Oechsle
Google

Michael Niemeyer
Google

Luc Van Gool
ETH Zürich
INSAIT

Martin R. Oswald
ETH Zürich
University of Amsterdam

Federico Tombari
Google
TU München

Abstract

3D Gaussian Splatting has emerged as a powerful representation of geometry and appearance for RGB-only dense Simultaneous Localization and Mapping (SLAM), as it provides a compact dense map representation while enabling efficient and high-quality map rendering. However, existing methods show significantly worse reconstruction quality than competing methods using other 3D representations, *e.g.* neural points clouds, since they either do not employ global map and pose optimization or make use of monocular depth. In response, we propose the first RGB-only SLAM system with a dense 3D Gaussian map representation that utilizes all benefits of globally optimized tracking by adapting dynamically to keyframe pose and depth updates by actively deforming the 3D Gaussian map. Moreover, we find that refining the depth updates in inaccurate areas with a monocular depth estimator further improves the accuracy of the 3D reconstruction. Our experiments on the Replica, TUM-RGBD, and ScanNet datasets indicate the effectiveness of globally optimized 3D Gaussians, as the approach achieves superior or on par performance with existing RGB-only SLAM methods in tracking, mapping and rendering accuracy while yielding small map sizes and fast runtimes. The source code is available at <https://github.com/eriksandroem/Splat-SLAM>.

1 Introduction

A common factor within the recent trend of dense SLAM is that the majority of works reconstruct a dense map by optimizing a neural implicit encoding of the scene, either as weights of an MLP [1, 57, 39, 45], as features anchored in dense grids [82, 42, 66, 67, 58, 3, 29, 83, 51], using hierarchical octrees [72], via voxel hashing [79, 78, 8, 49, 40], point clouds [18, 50, 30, 75] or axis-aligned feature planes [33, 47]. We have also seen the introduction of 3D Gaussian Splatting (3DGS) to the dense SLAM field [74, 24, 69, 38, 21].

Out of this 3D representation race there is, however, not yet a clear winner. In the context of dense SLAM, a careful modeling choice needs to be made to achieve accurate surface reconstruction as well as low tracking errors. Some takeaways can be deduced from the literature: neural implicit point cloud representations achieve state-of-the-art reconstruction accuracy [30, 75, 50], especially with RGBD input. At the same time, 3D Gaussian splatting methods yield the highest fidelity renderings [38, 74, 24, 21, 69] and show promise in the RGB-only setting due to their flexibility in optimizing the surface location [21, 38]. However, they are not leveraging any multi-view depth or geometric prior leading to poor geometry in the RGB-only setting. The majority of the aforementioned

*This work was conducted during an internship at Google.

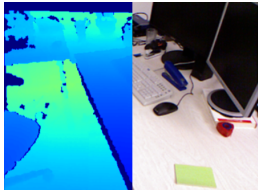
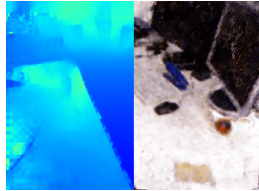
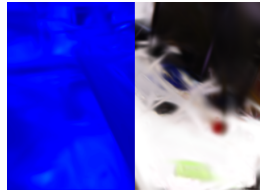
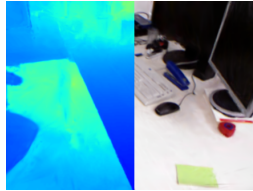
	Ground Truth	GIORIE-SLAM [75]	MonoGS [38]	Splat-SLAM (Ours)			
							
Depth L1 [cm]↓ PSNR↑		22.19	18.78	116.71	18.41	15.05	24.06
ATE RMSE [cm]↓		4.2	76.56	4.2			
Map Size [MB]↓		382.4	5.2	10.8			

Figure 1: **Splat-SLAM**. Our system yields accurate scene reconstruction (rendering depth L1) and rendering (PSNR) and on par tracking accuracy (ATE RMSE) to GIORIE-SLAM and map size to MonoGS. The results averaged over all keyframes. The scene is from TUM-RGBD [56] fr1 room.

works *only* deploy so called frame-to-model tracking, and do not implement global trajectory and map optimization, leading to excessive drift, especially in real world conditions. Instead, to this date, frame-to-frame tracking methods, coupled with loop closure and global bundle adjustment (BA) achieve state-of-the-art tracking accuracy [79, 78, 75]. However, they either use hierarchical feature grids [79, 78], not suitable for map deformations at *e.g.* loop closure as they require expensive reintegration strategies, or neural point clouds as in GIORIE-SLAM [75]. While the neural point cloud is straightforward to deform, the depth guided rendering leads to artifacts when the depth is noisy and the surface estimation can only be adjusted locally since the point locations are not optimized directly.

In this work we propose an RGB-only SLAM system that combines the strengths of frame-to-frame tracking using recurrent dense optical flow [61] with the fidelity of 3D Gaussians as the map representation [38] (see fig. 1). The point-based 3D Gaussian map enables online map deformations at loop closure and global BA. To enable accurate surface reconstruction, we leverage consistent so called proxy depth that combines multi-view depth estimation with learned monocular depth.

Our contribution comprises, for the first time, a SLAM pipeline encompassing all the following parts:

- A frame-to-frame RGB-only tracker with global consistency.
- A dense deformable 3D Gaussian map that adapts online to loop closure and global BA.
- A proxy depth map consisting of on-the-fly optimized multi-view depth and a monocular depth estimator leading to improved rendering and reconstruction quality.
- Improved map sizes and runtimes compared to other dense SLAM approaches.

2 Related Work

Dense Visual SLAM. Curless and Levoy [9] pioneered dense online 3D mapping with truncated signed distance functions, with KinectFusion [42] demonstrating real-time SLAM via depth maps. Enhancements like voxel hashing [43, 23, 44, 11, 40] and octrees [53, 72, 37, 5, 31] improved scalability, while point-based SLAM [68, 52, 4, 23, 25, 6, 76, 50, 30, 75] has also been effective. To address pose drift, globally consistent pose estimation and dense mapping techniques have been developed, often dividing the global map into submaps [4, 11, 15, 59, 40, 34, 22, 55, 7, 23, 48, 16, 2, 35, 59, 36, 30]. Loop detection triggers submap deformation via pose graph optimization [4, 34, 59, 40, 22, 13, 14, 27, 7, 17, 70, 52, 48, 16, 55, 63, 40, 18, 36, 30]. Sometimes global BA is used for refinement [11, 52, 4, 61, 70, 73, 40, 8, 59, 18]. 3D Gaussian SLAM with RGBD input has also been shown, but these methods do not consider global consistency via *e.g.* loop closure [74, 24, 69]. Other approaches to global consistency minimize reprojection errors directly, with DROID-SLAM [61] refining dense optical flow and camera poses iteratively, and recent enhancements like GO-SLAM [79], HI-SLAM [78], and GIORIE-SLAM [75] optimizing factor graphs for accurate tracking. For a recent survey on NeRF-inspired dense SLAM, see [62].

RGB-only Dense Visual SLAM. The majority of NeRF inspired dense SLAM works using only RGB cameras do not address the problem of global map consistency or requires expensive reintegration strategies via backpropagation [49, 8, 28, 81, 46, 79, 78, 20, 41, 19]. Instead, the concurrent GIORIE-

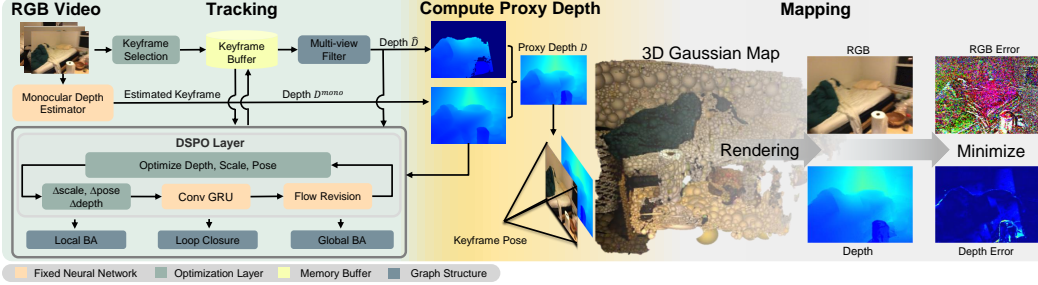


Figure 2: **Splat-SLAM Architecture.** Given an RGB input stream, we track and map each keyframe, initially estimating poses through local bundle adjustment (BA) using a DSPO (Disparity, Scale and Pose Optimization) layer. This layer integrates pose and depth estimation, enhancing depth with monocular depth. It further refines poses globally via online loop closure and global BA. The proxy depth map merges keyframe depths \tilde{D} from the tracking with monocular depth D^{mono} to fill gaps. Mapping employs a deformable 3D Gaussian map, optimizing its parameters through a re-rendering loss. Notably, the 3D map adjusts for global pose and depth updates before each mapping phase.

SLAM [75] uses a feature based point cloud which can adapt to global map changes in a straight forward way. However, redundant points are not pruned, leading to large map sizes. Furthermore, the depth guided sampling during rendering leads to rendering artifacts when noise is present in the estimated depth. MonoGS [38] and Photo-SLAM [21] pioneered RGB-only SLAM with 3D Gaussians. However, they lack proxy depth which prevents them from achieving high accuracy mapping. MonoGS [38] also lacks global consistency. Concurrent to our work, MoD-SLAM [80] uses an MLP to parameterize the map via a unique reparameterization.

3 Method

Splat-SLAM is a monocular SLAM system which tracks the camera pose while reconstructing the dense geometry of the scene in an online manner. This is achieved through the following steps: We first track the camera by performing local BA on selected keyframes by fitting them to dense optical flow estimates. The local BA optimizes the camera pose as well as the dense depth of the keyframe. For global consistency, when loop closure is detected, loop BA is performed on an extended graph including the loop nodes and edges (section 3.1). Interleaved with tracking, mapping is done on a progressively growing 3D Gaussian map which deforms online to the keyframe poses and so called proxy depth maps (section 3.2). For an overview of our method, see fig. 2.

3.1 Tracking

To predict the motion of the camera during scene exploration, we use a pretrained recurrent optical flow model [60] coupled with a Disparity, Scale and Pose Optimization (DSPO) layer [75] to jointly optimize camera poses and per pixel disparities. In the following, we describe this process in detail.

Optimization is done with the Gauss-Newton algorithm over a factor graph $G(V, E)$, where the nodes V store the keyframe pose and disparity, and edges E store the optical flow between keyframes. Odometry keyframe edges are added to G by computing the optical flow to the last added keyframe. If the mean flow is larger than a threshold $\tau \in \mathbb{R}$, the new keyframe is added to G . Edges for loop closure and global BA are discussed later. Importantly, the same objective is optimized for local BA, loop closure and global BA, but over factor graphs with different structures.

The DSPO layer consists of two optimization objectives that are optimized alternatively. The first objective, typically termed Dense Bundle Adjustment (DBA) [61] optimizes the pose and disparity of the keyframes jointly, eq. (1). Specifically, the objective is optimized over a local graph defined within a sliding window over the current frame.

$$\arg \min_{\omega, d} \sum_{(i,j) \in E} \left\| \tilde{p}_{ij} - K\omega_j^{-1}(\omega_i(1/d_i)K^{-1}[p_i, 1]^T) \right\|_{\Sigma_{ij}}^2, \quad (1)$$

with $\tilde{p}_{ij} \in \mathbb{R}^{(W \times H \times 2) \times 1}$ being the flattened predicted pixel coordinates when the pixels $p_i \in \mathbb{R}^{(W \times H \times 2) \times 1}$ from keyframe i are projected into keyframe j using optical flow. Further, K is the

camera intrinsics, ω_j and ω_i the camera-to-world extrinsics for keyframes j and i , d_i the disparity of pixel p_i and $\|\cdot\|_{\Sigma_{ij}}$ is the Mahalanobis distance with diagonal weighting matrix Σ_{ij} . Each weight denotes the confidence of the optical flow prediction for each pixel in \tilde{p}_{ij} . For clarity of the presentation, we omit homogeneous coordinates.

The second objective introduces monocular depth D^{mono} as two additional data terms. The monocular depth D^{mono} is predicted at runtime by a pretrained relative depth DPT model [12].

$$\begin{aligned} \arg \min_{d^h, \theta, \gamma} \sum_{(i,j) \in E} \|\tilde{p}_{ij} - K\omega_j^{-1}(\omega_i(1/d_i^h)K^{-1}[p_i, 1]^T)\|_{\Sigma_{ij}}^2 \\ + \alpha_1 \sum_{i \in V} \|d_i^h - (\theta_i(1/D_i^{\text{mono}}) + \gamma_i)\|^2 + \alpha_2 \sum_{i \in V} \|d_i^l - (\theta_i(1/D_i^{\text{mono}}) + \gamma_i)\|^2. \end{aligned} \quad (2)$$

Here, the optimizable parameters are the scales $\theta \in \mathbb{R}$, shifts $\gamma \in \mathbb{R}$ and a subset of the disparities d^h classified as being high error (explained later). This is done since the monocular depth is only deemed useful where the multi-view disparity d_i optimization is inaccurate. Furthermore, $\alpha_1 < \alpha_2$, which is done to ensure that the scales θ and shifts γ are optimized with the preserved low error disparities d^l . The scale θ_i and shift γ_i are initialized using least squares fitting

$$\{\theta_i, \gamma_i\} = \arg \min_{\theta, \gamma} \sum_{(u,v)} \left((\theta(1/D_i^{\text{mono}}) + \gamma) - d_i^l \right)^2. \quad (3)$$

Equation (1) and eq. (2) are optimized alternately to avoid the scale ambiguity encountered if d , θ , γ and ω are optimized jointly.

Next, we describe how high and low error disparities are classified. For a given disparity map d_i (separated into low and high error parts $\{d_i^l, d_i^h\}$) for frame i , we denote the corresponding depth $\tilde{D}_i = 1/d_i$. Pixel correspondences (u, v) and (\hat{u}, \hat{v}) between keyframes i and j respectively are established by warping (u, v) into frame j with depth \tilde{D}_i as

$$p_i = \omega_i \tilde{D}_i(u, v) K^{-1}[u, v, 1]^T, \quad [\hat{u}, \hat{v}, 1]^T \propto K\omega_j^{-1}[p_i, 1]^T. \quad (4)$$

The corresponding 3D point to (\hat{u}, \hat{v}) is computed from the depth at (\hat{u}, \hat{v}) as

$$p_j = \omega_j \tilde{D}_j(\hat{u}, \hat{v}) K^{-1}[\hat{u}, \hat{v}, 1]^T. \quad (5)$$

If the L2 distance between p_i and p_j is smaller than a threshold, the depth $\tilde{D}_i(u, v)$ is consistent between i and j . By looping over all keyframes except i , the global two-view consistency n_i can be computed for frame i as

$$n_i(u, v) = \sum_{\substack{k \in \text{KFs}, \\ k \neq i}} \mathbb{1} \left(\|p_i - p_k\|_2 < \eta \cdot \text{average}(\tilde{D}_i) \right). \quad (6)$$

Here, $\mathbb{1}(\cdot)$ is the indicator function and $\eta \in \mathbb{R}_{\geq 0}$ is a hyperparameter and n_i is the total two-view consistency for pixel (u, v) in keyframe i . $\tilde{D}_i(u, v)$ is valid if n_i is larger than a threshold.

Loop Closure. To mitigate scale and pose drift, we incorporate loop closure along with online global bundle adjustment (BA) in addition to local window frame tracking. Loop detection is achieved by calculating the mean optical flow magnitude between the current active keyframes (within the local window) and all previous keyframes. Two criteria are evaluated for each keyframe pair: First, the optical flow must be below a specified threshold τ_{loop} , ensuring sufficient co-visibility between the views. Second, the time interval between the frames must exceed a predefined threshold τ_t to prevent the introduction of redundant edges into the graph. When both criteria are met, a unidirectional edge is added to the graph. During the loop closure optimization process, only the active keyframes and their connected loop nodes are optimized to keep the computational load manageable.

Global BA. For the online global BA, a separate graph that includes all keyframes up to the present is constructed. Edges are introduced based on the temporal and spatial relationships between the keyframes, as outlined in [79]. Following the approach detailed in [75], we execute online global BA every 20 keyframes. To maintain numerical stability, the scales of the disparities and poses are normalized prior to each global BA optimization. This normalization involves calculating the average disparity \bar{d} across all keyframes and then adjusting the disparity to $d_{\text{norm}} = d/\bar{d}$ and the pose translation to $t_{\text{norm}} = \bar{d}t$.

3.2 Deformable 3D Gaussian Scene Representation

We adopt a 3D Gaussian Splatting representation [26] which deforms under DSPO or loop closure optimizations to achieve global consistency. Thus, the scene is represented by a set $\mathcal{G} = \{g_i\}_{i=1}^N$ of 3D Gaussians. Each Gaussian primitive g_i , is parameterized by a covariance matrix $\Sigma_i \in \mathbb{R}^{3 \times 3}$, a mean $\boldsymbol{\mu}_i \in \mathbb{R}^3$, opacity $o_i \in [0, 1]$, and color $\mathbf{c}_i \in \mathbb{R}^3$. All attributes of each Gaussian are optimized through back-propagation. The density function of a single Gaussian is described as

$$g_i(\mathbf{x}) = \exp\left(-\frac{1}{2}(\mathbf{x} - \boldsymbol{\mu}_i)^\top \Sigma_i^{-1}(\mathbf{x} - \boldsymbol{\mu}_i)\right). \quad (7)$$

Here, the spatial covariance Σ_i defines an ellipsoid and is decomposed as $\Sigma_i = R_i S_i S_i^T R_i^T$, where $S_i = \text{diag}(s_i) \in \mathbb{R}^{3 \times 3}$ is the spatial scale and $R_i \in \mathbb{R}^{3 \times 3}$ represents the rotation.

Rendering. Rendering color and depth from \mathcal{G} , given a camera pose, involves first projecting (known as ‘‘splatting’’) 3D Gaussians onto the 2D image plane. This is done by projecting the covariance matrix Σ and mean $\boldsymbol{\mu}$ as $\Sigma' = JR\Sigma R^T J^T$ and $\boldsymbol{\mu}' = K\omega^{-1}\boldsymbol{\mu}$, where R is the rotation component of world-to-camera extrinsics ω^{-1} and J is the Jacobian of the affine approximation of the projective transformation [84]. The final pixel color C and depth D^r at pixel \mathbf{x}' is computed by blending 3D Gaussian splats that overlap at a given pixel, sorted by their depth as

$$C = \sum_{i \in \mathcal{N}} \mathbf{c}_i \alpha_i \prod_{j=1}^{i-1} (1 - \alpha_j) \quad D^r = \sum_{i \in \mathcal{N}} \hat{d}_i \alpha_i \prod_{j=1}^{i-1} (1 - \alpha_j), \quad (8)$$

where \hat{d}_i is the z-axis depth of the center of the i -th 3D Gaussian and the final opacity α_i is the product of the opacity o_i and the 2D Gaussian density as

$$\alpha_i = o_i \exp\left(-\frac{1}{2}(\mathbf{x}' - \boldsymbol{\mu}'_i)^\top \Sigma_i'^{-1}(\mathbf{x}' - \boldsymbol{\mu}'_i)\right). \quad (9)$$

Map Initialization. For every new keyframe, we adopt the RGBD strategy of MonoGS [38] for adding new Gaussians to the unexplored scene space. As we do not have access to a depth sensor, we construct a proxy depth map D by combining the inlier multi-view depth \tilde{D} and the monocular depth D^{mono} as

$$D(u, v) = \begin{cases} \tilde{D}(u, v) & \text{if } \tilde{D}(u, v) \text{ is valid} \\ \theta D^{\text{mono}}(u, v) + \gamma & \text{otherwise} \end{cases} \quad (10)$$

Here, θ and γ are computed as in eq. (3) but using depth instead of disparity.

Keyframe Selection and Optimization. Apart from the keyframe selection based on a mean optical flow threshold τ , we additionally adopt the keyframe selection strategy from [38] to avoid mapping redundant frames.

To optimize the 3D Gaussian parameters, we batch the parameter updates to a local window similar to [38] and apply a photometric and geometric loss to the proxy depth as well as a scale regularizer to avoid artifacts from elongated Gaussians. Inspired by [38], we further use exposure compensation by optimizing an affine transformation for each keyframe. The final loss is

$$\min_{\mathcal{G}, \mathbf{a}, \mathbf{b}} \sum_{k \in \text{KFs}} \frac{\lambda}{N_k} |(a_k C_k + b_k) - C_k^{\text{gt}}|_1 + \frac{1 - \lambda}{N_k} |D_k^r - D_k|_1 + \frac{\lambda_{\text{reg}}}{|\mathcal{G}|} \sum_i |s_i - \tilde{s}_i|, \quad (11)$$

where KFs contains the set of keyframes in the local window, N_k is the number of pixels per keyframe, λ and λ_{reg} are hyperparameters, $\mathbf{a} = \{a_1, \dots, a_k, \dots\}$ and $\mathbf{b} = \{b_1, \dots, b_k, \dots\}$ are the parameters for the exposure compensation and \tilde{s} is the mean scaling, repeated over the three dimensions.

Map Deformation. Since our tracking framework is globally consistent, changes in the keyframe poses and proxy depth maps need to be accounted for in the 3D Gaussian map by a non-rigid deformation. Though the Gaussian means are directly optimized, one could in theory let the optimizer deform the map as refined poses and proxy depth maps are provided. We find, however, that in particular rendering is aided by actively deforming the 3D Gaussian map. We apply the deformation to all Gaussians which receive updated poses and depths before mapping.

Each Gaussian g_i is associated with a keyframe that anchored it to the map \mathcal{G} . Assume that a keyframe with camera-to-world pose ω and proxy depth D is updated such that $\omega \rightarrow \omega'$ and $D \rightarrow D'$. We

Metric	GO-SLAM [79]	NICER-SLAM [81]	MoD-SLAM* [28]	Photo-SLAM [21]	Mono-GS [38]	GIORIE-SLAM* [75]	Q-SLAM* [46]	Ours
PSNR↑	22.13	25.41	27.31	33.30	31.22	31.04	32.49	36.45
SSIM↑	0.73	0.83	0.85	0.93	0.91	0.91	0.89	0.95
LPIPS↓	-	0.19	-	-	0.21	0.12	0.17	0.06
ATE RMSE↓	0.39	1.88	0.35	1.09	14.54	0.35	-	0.35

Table 1: **Rendering and Tracking Results on Replica [54] for RGB-Methods.** Our method outperforms all methods on rendering and performs on par for tracking accuracy. Results are from [62] except ours (average over 8 scenes). Best results are highlighted as **first**, **second**, **third**.

update the mean, scale and rotation of all Gaussians g_i associated with the keyframe. Association is determined by what keyframe added the Gaussian to the scene. The mean μ_i is projected into ω to find the pixel correspondence (u, v) . Since the Gaussians are not necessarily anchored on the surface, instead of re-anchoring the mean at D' , we opt to shift the mean by $D'(u, v) - D(u, v)$ along the optical axis. We update R_i and s_i accordingly as

$$\mu'_i = \left(1 + \frac{D'(u, v) - D(u, v)}{(\omega^{-1}\mu_i)_z}\right)\omega'\omega^{-1}\mu_i, R'_i = R'R^{-1}R_i, s'_i = \left(1 + \frac{D'(u, v) - D(u, v)}{(\omega^{-1}\mu_i)_z}\right)s_i. \quad (12)$$

Here, $(\cdot)_z$ denotes the z-axis depth. For Gaussians which project into pixels with missing depth or outside the viewing frustum, we *only* rigidly deform them. After the final global BA optimization, we additionally deform the Gaussian map and perform a set of final refinements (see suppl. material).

4 Experiments

We first describe our experimental setup and then evaluate our method against state-of-the-art dense RGB and RGBD SLAM methods on Replica [54] as well as the real world TUM-RGBD [56] and the ScanNet [10] datasets. For more experiments and details, we refer to the supplementary material.

Implementation Details. For the proxy depth, we use $\eta = 0.01$ to filter points and use the condition $n_c \geq 2$ to ensure multi-view consistency. For the mapping loss function, we use $\lambda = 0.8$, $\lambda_{reg} = 10.0$. We use 60 iterations during mapping. For tracking, we use $\alpha_1 = 0.01$ and $\alpha_2 = 0.1$ as weights for the DSPO layer. We use the flow threshold $\tau = 4.0$ on ScanNet, $\tau = 3.0$ on TUM-RGBD and $\tau = 2.25$ on Replica. The threshold for loop detection is $\tau_{loop} = 25.0$. The time interval threshold is $\tau_t = 20$. We conducted the experiments on a cluster with an NVIDIA A100 GPU.

Evaluation Metrics. For rendering we report PSNR, SSIM [65] and LPIPS [77] on the rendered keyframe images against the sensor images. For reconstruction, we first extract the meshes with marching cubes [32] as in [50] and evaluate the meshes using accuracy [cm], completion [cm] and completion ratio [%] (threshold 5 cm) against the ground truth meshes. We also report the re-rendering depth L1 [cm] metric to the ground truth sensor depth as in [49]. We use ATE RMSE [cm] [56] to evaluate the estimated trajectory.

Datasets. We use the RGBD trajectories from [57] captured from the synthetic Replica dataset [54]. We also test on real-world data using the TUM-RGBD [56] and the ScanNet [10] datasets.

Baseline Methods. We compare our method to numerous published and concurrent works on dense RGB and RGBD SLAM. Concurrent works are denoted with an asterix*. The main baselines are GIORIE-SLAM [75] and MonoGS [38].

Rendering. In tab. 1, we evaluate the rendering performance on Replica [54] and find that our method performs superior among all baseline RGB-methods. Tab. 2 and tab. 3 show the rendering accuracy on the ScanNet [10] and TUM-RGBD [56] datasets. In particular, we outperform existing RGB-only works with a clear margin, while even beating the currently best RGBD method, Gaussian-SLAM [74] on most metrics, despite the fact that we do not implement view-dependent rendering in the form of spherical harmonics. We attribute this to our deformable 3D Gaussian map, optimized with strong proxy depth along a globally consistent tracking backend. In fig. 3 and fig. 1 we show renderings on the real-world ScanNet [10] and TUM-RGBD [56] datasets. Due to high tracking errors, MonoGS [38] performs poorly on some scenes, yet fails to achieve the same fidelity as our method when the tracking error is low, as a result of the weak geometric constraints during optimization. Our method avoids the artifacts produced by GIORIE-SLAM [75] and yields high quality renderings.

Method	Metric	0000	0059	0106	0169	0181	0207	Avg.
<i>RGB-D Input</i>								
SplaTaM [24]	PSNR↑	19.33	19.27	17.73	21.97	16.76	19.80	19.14
	SSIM↑	0.66	0.79	0.69	0.78	0.68	0.70	0.72
	LPIPS↓	0.44	0.29	0.38	0.28	0.42	0.34	0.36
MonoGS [38]	PSNR↑	18.70	20.91	19.84	22.16	22.01	18.90	20.42
	SSIM↑	0.71	0.79	0.81	0.78	0.82	0.75	0.78
	LPIPS↓	0.48	0.32	0.32	0.34	0.42	0.41	0.38
Gaussian-SLAM [74]	PSNR↑	28.54	26.21	26.26	28.60	27.79	28.63	27.67
	SSIM↑	0.93	0.93	0.93	0.92	0.92	0.91	0.92
	LPIPS↓	0.27	0.21	0.22	0.23	0.28	0.29	0.25
<i>RGB Input</i>								
GO-SLAM [79]	PSNR↑	15.74	13.15	14.58	14.49	15.72	15.37	14.84
	SSIM↑	0.42	0.32	0.46	0.42	0.53	0.39	0.42
	LPIPS↓	0.61	0.60	0.59	0.57	0.62	0.60	0.60
MonoGS [38]	PSNR↑	16.91	19.15	18.57	20.21	19.51	18.37	18.79
	SSIM↑	0.62	0.69	0.74	0.74	0.75	0.70	0.71
	LPIPS↓	0.70	0.51	0.55	0.54	0.63	0.58	0.59
GIORIE-SLAM* [75]	PSNR↑	23.42	20.66	20.41	25.23	21.28	23.68	22.45
	SSIM↑	0.87	0.87	0.83	0.84	0.91	0.76	0.85
	LPIPS↓	0.26	0.31	0.31	0.21	0.44	0.29	0.30
Splat-SLAM (Ours)	PSNR↑	28.68	27.69	27.70	31.14	31.15	30.49	29.48
	SSIM↑	0.83	0.87	0.86	0.87	0.84	0.84	0.85
	LPIPS↓	0.19	0.15	0.18	0.15	0.23	0.19	0.18

Table 2: **Rendering Performance on ScanNet [10]**. Our method performs even better or on par with all RGB-D methods. We take the numbers for SplaTaM and Gaussian-SLAM from [74].

Method	Method	f1/desk	f2/xyz	f3/off	f1/desk2	f1/room	Avg.
<i>RGB-D Input</i>							
SplaTaM [24]	PSNR↑	22.00	24.50	21.90	-	-	-
	SSIM↑	0.86	0.95	0.88	-	-	-
	LPIPS↓	0.23	0.10	0.20	-	-	-
Gaussian-SLAM [74]	PSNR↑	24.01	25.02	26.13	23.15	22.98	24.26
	SSIM↑	0.92	0.92	0.94	0.91	0.89	0.92
	LPIPS↓	0.18	0.19	0.14	0.20	0.24	0.19
<i>RGB Input</i>							
Photo-SLAM [21]	PSNR↑	20.97	21.07	19.59	-	-	-
	SSIM↑	0.74	0.73	0.69	-	-	-
	LPIPS↓	0.23	0.17	0.24	-	-	-
MonoGS [38]	PSNR↑	19.67	16.17	20.63	19.16	18.41	18.81
	SSIM↑	0.73	0.72	0.77	0.66	0.64	0.70
	LPIPS↓	0.33	0.31	0.34	0.48	0.51	0.39
GIORIE-SLAM* [75]	PSNR↑	20.26	25.62	21.21	19.09	18.78	20.99
	SSIM↑	0.79	0.72	0.72	0.92	0.73	0.77
	LPIPS↓	0.31	0.09	0.32	0.38	0.38	0.30
Splat-SLAM (Ours)	PSNR↑	25.61	29.53	26.05	23.98	24.06	25.85
	SSIM↑	0.84	0.90	0.84	0.81	0.80	0.84
	LPIPS↓	0.18	0.08	0.20	0.23	0.24	0.19

Table 3: **Rendering Performance on TUM-RGBD [56]**. Our method performs competitively or better than RGB-D methods. For all RGB-D methods, we take the numbers from [74].

Reconstruction. We show quantitative and qualitative results on the Replica [54] dataset in tab. 4 and fig. 4 respectively. Our method achieves the best performance on all metrics. Qualitatively, we show normal shaded meshes from different viewpoints. Our method can reconstruct finer details than existing works, especially around thin structures (*e.g.* second row), where our strong proxy depth coupled with the 3D Gaussian map representation yields superior depth rendering, which directly influences the mesh quality. In contrast, *e.g.* GIORIE-SLAM [75] uses depth guided volume rendering, which is sensitive to input depth noise, resulting in inconsistent depth rendering with floating artifacts. MonoGS [38] suffers significantly from the lack of proxy depth, visible in all scenes. Fig. 1 shows depth rendering on the real-world TUM-RGBD [56] room scene. We compute the average depth L1 error over all keyframes, achieving 15.05 cm, beating existing works.

Ablation Study. In tab. 5, we conduct a set of ablation studies related to our method, by enabling and disabling certain parts. We find that the combination of filtered multiview depth completed with monocular depth yields the best performance in terms of rendering and reconstruction metrics.

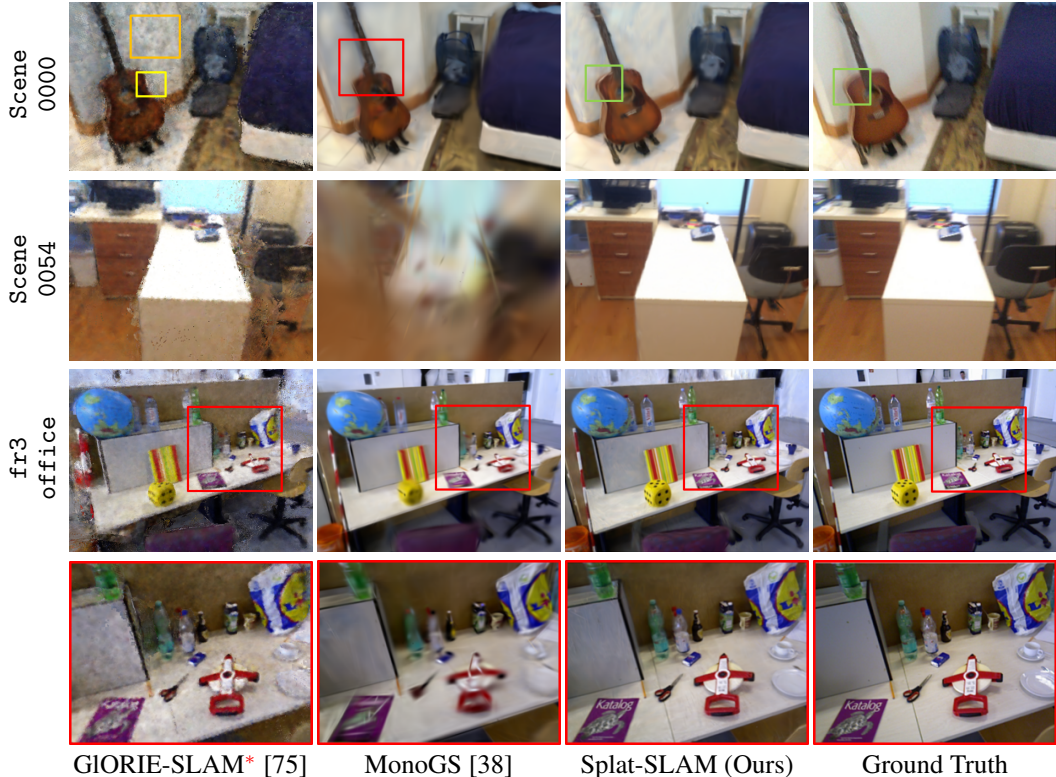


Figure 3: **Rendering Results on ScanNet [10] and TUM-RGBD [56].** Our method yields better rendering quality than GIORIE-SLAM and MonoGS. Top row: the orange box shows artifacts from GIORIE-SLAM, partly due to the depth guided volume rendering. The yellow box shows an area with redundant floating points. The red box shows a rendering distortion, likely from the large trajectory error. The green boxes show that our method fuses information from multiple views to avoid motion blur, present in the input. Fourth row: The rendering is from the pose of the red box in the third row.

Metrics	NeRF-SLAM [62]	DIM-SLAM [28]	GO-SLAM [79]	NICER-SLAM [81]	HI-SLAM [78]	MoD-SLAM* [80]	GIORIE-SLAM* [75]	MonoGS [38]	Q-SLAM* [46]	Ours
Render Depth L1↓	4.49	-	-	-	-	-	-	27.24	2.76	2.41
Accuracy ↓	-	4.03	3.81	3.65	3.62	2.48	2.96	30.61	-	2.43
Completion ↓	-	4.20	4.79	4.16	4.59	-	3.95	12.19	-	3.64
Comp. Rat. ↑	-	79.60	78.00	79.37	80.60	-	83.72	40.53	-	84.69

Table 4: **Reconstruction Results on Replica [54] for RGB-Methods.** Our method outperforms existing works on all metrics. Results are averaged over 8 scenes.

Memory and Runtime. In tab. 6, we evaluate the peak GPU memory usage, map size and runtime of our method. We achieve a comparable GPU memory usage with GO-SLAM [79] and SplaTaM [24]. Our map size is similar to MonoGS [38] and much smaller than GIORIE-SLAM, which does not prune redundant neural points. In fig. 1 we also show similar map size to MonoGS on the real-world TUM-RGBD [56] room scene. Regarding runtime, we are faster than SplaTaM and GIORIE-SLAM and comparable to MonoGS. GO-SLAM has the fastest runtime, but as shown in tab. 1 and tab. 4, it sacrifices rendering and reconstruction quality for speed.

Limitations. We currently do not model the appearance with spherical harmonics, since it only yields a marginal gains in rendering accuracy, while requiring more memory. It is straightforward to add. We only make use of globally optimized frame-to-frame tracking, which fails to leverage frame-to-model queues from the 3D Gaussian map. Another limitation is that our construction of the final proxy depth D is quite simple and does not fuse the monocular and keyframe depths in an informed manner, *e.g.* using normal consistency. Finally, as future work, it is interesting to study how surface regularization can be enforced via *e.g.* quadric surface elements as in [46].

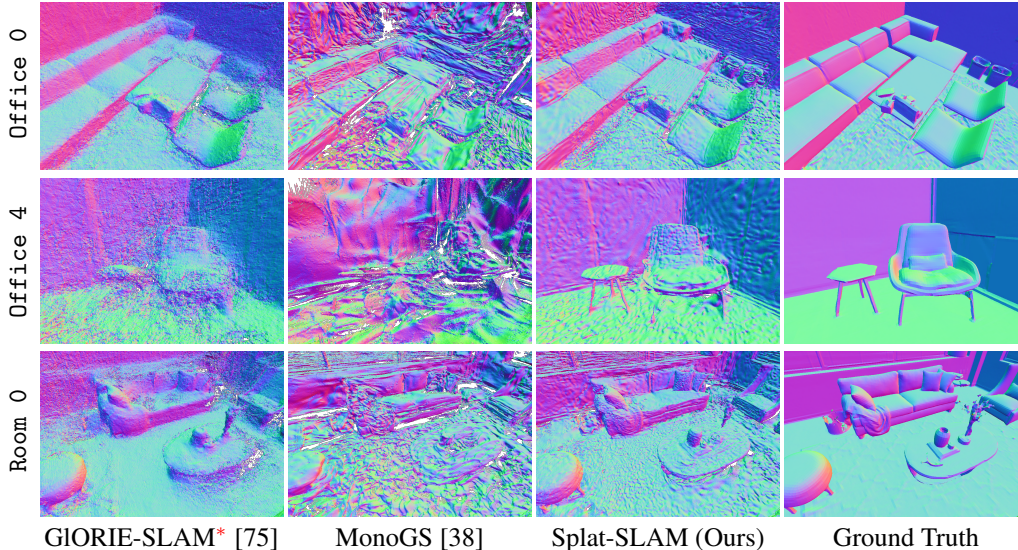


Figure 4: **Reconstruction Results on Replica [54] on Normal Shaded Meshes.** Our method achieves higher geometric accuracy compared to existing works. In particular, GIORIE-SLAM suffers from floating point artifacts (*e.g.* second row) where our method reconstructs even the individual legs of the table. MonoGS suffers significantly from a lack of proxy depth, despite multiview optimization.

Mono Depth	Multiview Depth	Multiview Filtering	PSNR [dB] ↑	Acc. [cm] ↓	Comp. [cm] ↓	Comp. Ratio [cm] ↑
✓	✗	✗	36.02	3.62	4.08	81.16
✗	✓	✓	36.17	2.64	4.73	80.12
✗	✓	✗	36.21	18.71	4.06	80.29
✓	✓	✓	36.45	2.43	3.64	84.69

Table 5: **Ablation Study on Replica [54].** We show that the combination of filtered multiview depth completed with monocular depth yields the best performance on all metrics. Mono Depth refers to D^{mono} , Multiview Depth refers to \tilde{D} and Multiview Filtering means enabling eq. (6). All results are averaged over 8 scenes.

	GO-SLAM [79]	SplaTAM [24]	GIORIE-SLAM* [75]	MonoGS [38]	Ours
GPU Usage [GiB]	18.50	18.54	15.22	14.62	17.57
Map Size [MB]	-	-	114.0	6.8	6.5
Avg. FPS	8.36	0.14	0.23	0.32	1.24

Table 6: **Memory and Running Time Evaluation on Replica [54] room0.** Our peak memory usage and runtime are comparable to existing works. We take the numbers from [62] except for ours and MonoGS and we add the Map Size, which denotes the size of the final 3D representation. GPU Usage denotes the peak usage during runtime. All methods are evaluated on an NVIDIA RTX 3090 GPU using single threading for fairness.

5 Conclusion

We proposed Splat-SLAM, a dense RGB-only SLAM system which uses a deformable 3D Gaussian map for mapping and globally optimized frame-to-frame tracking via optical flow. Importantly, the inclusion of monocular depth into the tracking loop, to refine the scale and to correct the erroneous keyframe depth predictions, leads to better rendering and mapping. By using the monocular depth for completion, mapping is further improved. Our experiments demonstrate that Splat-SLAM outperforms existing solutions regarding reconstruction and rendering accuracy while being on par or better with respect to tracking as well as runtime and memory usage.

Supplementary Material

Splat-SLAM: Globally Optimized RGB-only SLAM with 3D Gaussians

Erik Sandström* **Keisuke Tateno** **Michael Oechsle** **Michael Niemeyer**
 Google Google Google Google
 ETH Zürich

Luc Van Gool **Martin R. Oswald** **Federico Tombari**
 ETH Zürich ETH Zürich Google
 INSAIT University of Amsterdam TU München

This supplementary material accompanies the main paper and provides more details on the methodology and additional experimental results.

A Method

We describe further details about our method that were left out from the main paper.

Comparison to Existing Works. To further clarify the differences between our method and existing 3DGS SLAM works, we classify each method in tab. S8 based on important characteristics. It shows that our work is the first to include loop closure, proxy depth, RGB-only and online 3D Gaussian deformations.

	RGB-only	Loop Closure	Proxy Depth	Online 3DGS Deformations
GS-SLAM [69]	✗	✗	✓	✗
Gaussian-SLAM [74]	✗	✗	✓	✗
SplaTaM [24]	✗	✗	✓	✗
MonoGS [38]	✓	✗	✗	✗
Photo-SLAM [21]	✓	✓	✗	✗
Splat-SLAM (ours)	✓	✓	✓	✓

Table S8: **Method Classification.** We show that our method is the first to combine 3D Gaussian SLAM with loop closure, proxy depth and online 3D Gaussian map deformations in an RGB-only SLAM system.

Map Initialization. With map initialization, we refer to the process of anchoring new Gaussians during scene exploration. For every new keyframe to be mapped, we adopt the strategy that MonoGS [38] uses in pure RGBD mode. It works by unprojecting the depth reading per pixel to 3D and then downsampling this point cloud by a factor θ . New Gaussians are then assigned their means as the point cloud. The rotations are initialized to identity, the opacity to 0.5 and the scales are initialized related to their distance to the nearest neighbor point in the point cloud.

Keyframe Selection and Local Windowing. As mentioned in the main paper, we adopt the keyframe selection strategy from MonoGS [38]. We describe this strategy in the following.

Keyframes are selected based on the covisibility of the Gaussians. Between two keyframes i and j , the covisibility is defined using the Intersection over Union (IOU) and Overlap Coefficient (OC):

$$\text{IOU}_{\text{cov}}(i, j) = \frac{|\mathcal{G}_v^i \cap \mathcal{G}_v^j|}{|\mathcal{G}_v^i \cup \mathcal{G}_v^j|}, \quad (16)$$

*This work was conducted during an internship at Google.

$$\text{OC}_{\text{cov}}(i, j) = \frac{|\mathcal{G}_v^i \cap \mathcal{G}_v^j|}{\min(|\mathcal{G}_v^i|, |\mathcal{G}_v^j|)}, \quad (17)$$

where \mathcal{G}_v^i are the Gaussians visible in keyframe i , based on the following definition of visibility. A Gaussian is seen as visible from a camera pose if it is used in the rasterization pipeline when rendering and if the accumulated transmittance $\prod_{j=1}^{i-1} (1 - \alpha_j)$ has not yet reached 0.5.

A keyframe i is added to the keyframe window KFs if, given the last keyframe j , $\text{IOU}_{\text{cov}}(i, j) < k_{\text{fcov}}$ or if the relative translation $t_{ij} > k_{\text{fm}} \hat{D}_i$, where \hat{D}_i is the median depth of frame i . For Replica, $k_{\text{fcov}} = 0.95$, $k_{\text{fm}} = 0.04$ and for TUM and ScanNet, $k_{\text{fcov}} = 0.90$, $k_{\text{fm}} = 0.08$. The registered keyframe j in KFs is removed if $\text{OC}_{\text{cov}}(i, j) < k_{\text{fc}}$, where keyframe i is the latest added keyframe. For all datasets, the cutoff is set to $k_{\text{fc}} = 0.3$. The size of the keyframe window is set to $|\text{KFs}| = 10$ for Replica and $|\text{KFs}| = 8$ for TUM and ScanNet.

Pruning and Densification We also follow [38] when it comes to Gaussian pruning and densification. Pruning is done based on the visibility: if new Gaussians inserted within the last 3 keyframes are not visible by at least 3 other frames in the keyframe window KFs, they are removed. Visibility-based pruning is only done when the keyframe window KFs is full. Additionally, every 150 mapping iterations, Gaussians with opacity lower than 0.7 are removed globally. Also Gaussians which project in 2D with a too large scale are removed. Densification is done as in [26], also at an interval of every 150 mapping iterations.

Final Refinement. Similar to GIORIE-SLAM [75], which performs a final refinement after the last final global BA at the end of the trajectory, we also perform a few refinement iterations after the last final global BA. Also MonoGS [38] performs a set of final iterations at the end of the SLAM trajectory to refine the colors.

Our refinement strategy is straight forward. We disable pruning and densification of the Gaussians and perform a set of optimization iterations β using the same loss function as in the main paper, but only sampling random single frames per iteration.

Differences to GIORIE-SLAM. We briefly discuss some differences to GIORIE-SLAM [75] not covered in the main paper. GIORIE-SLAM uses an additional point cloud called P_d consisting of all inlier multi-view depth maps unprojected into a point cloud. We found that this is not needed and it saves memory and compute to not use it. GIORIE-SLAM also re-anchors the neural points at the depth reading. We do not do this as the Gaussians do not necessarily lie on the surface exactly. Finally, GIORIE-SLAM requires input depth to guide the sampling of points to render color and depth. If the depth is noisy or if the map is used for tracking (*i.e.* frame-to-model tracking), the depth guiding strategy is not favorable as it leads to artifacts when sampling the wrong points (when noisy depth is encountered) and to a much smaller basin of convergence when tracking (because the rendering is conditioned on the current view point). With 3D Gaussians, we can avoid depth guidance during rendering.

B More Experiments

To accompany the evaluations provided in the main paper, we provide further experiments in this section.

Implementation Details. As the point cloud downsampling factor, we use $\theta = 32$ for all frames but the first frame where $\theta = 16$ is used. We use $\beta = 2000$, the number of iterations for the final refinement optimization, on the Replica dataset and $\beta = 26000$ on the TUM-RGBD [56] and ScanNet [10] datasets (same as MonoGS [38]). We benchmark the runtime on an AMD Ryzen Threadripper Pro 3945WX 12-Cores with an NVIDIA GeForce RTX 3090 Ti with 24 GB of memory. For the remaining hyperparameters, we refer to MonoGS [38] for the Gaussian mapping and GIORIE-SLAM for tracking [75].

A Note on Rendering and Runtime with MonoGS. By default, MonoGS [38] does not evaluate the rendering error on the mapped keyframes nor implement the exposure compensation during rendering evaluation. To compare our results fairly to MonoGS, we implement these details and run the experiments with these settings enabled. Further, we report the runtime for MonoGS using a single process (same as us) compared to the reported number in the paper, which was using multiple processes at once.

A Note on Gaussian Deformation with Photo-SLAM. Though not fully clear from reading the paper, after discussing with the authors of Photo-SLAM [21], we find that they do, in fact, not deform the Gaussians as a result of global BA or loop closure. They found this to be unstable in their experiments. This suggests that our deformation strategy is non-trivial.

Justification of Monocular Depth Estimator. There are already numerous monocular depth estimators, but most of them are limited by speed, memory or quality. We use Omnidata [12] since empirically we found it still provides the best trade-off between output performance and runtime. We also tested our system with Depth Anything [71], but found that it was marginally worse in terms of the final reconstructed mesh accuracy.

B.1 Tracking on ScanNet and TUM-RGBD

We do not put the results on tracking for ScanNet and TUM-RGBD since we use the tracking framework from GIORIE-SLAM [75], but we provide the numbers here. Tab. S9 and tab. S10 show the tracking accuracy of the estimated trajectory on ScanNet [10] and TUM-RGBD [56] respectively. Our method shows competitive results in every single scene and gives the best average value among the RGB and RGB-D methods.

Method	0000	0059	0106	0169	0181	0207	Avg.-6	0054	0233	Avg.-8
<i>RGB-D Input</i>										
NICE-SLAM [82]	12.0	14.0	7.9	10.9	13.4	6.2	10.7	20.9	9.0	11.8
Co-SLAM [64]	7.1	11.1	9.4	5.9	11.8	7.1	8.7	-	-	-
ESLAM [33]	7.3	8.5	7.5	6.5	9.0	5.7	7.4	36.3	4.3	10.6
MonoGS[38]	16.1	6.4	8.1	8.7	26.4	9.2	12.5	20.6	13.1	13.6
<i>RGB Input</i>										
MonoGS[38]	149.2	96.8	155.5	140.3	92.6	101.9	122.7	206.4	89.1	129.0
GO-SLAM [79]	5.9	8.3	8.1	8.4	8.3	6.9	7.7	13.3	5.3	8.1
HI-SLAM[78]	6.4	7.2	6.5	8.5	7.6	8.4	7.4	-	-	-
Q-SLAM* [46]	5.8	8.5	8.4	8.7	8.8	-	-	12.6	5.3	-
GIORIE-SLAM* [75]	5.5	9.1	7.0	8.2	8.3	7.5	7.6	9.4	5.1	7.5
Ours	5.5	9.1	7.0	8.2	8.3	7.5	7.6	9.4	5.1	7.5

Table S9: **Tracking Accuracy ATE RMSE [cm] ↓ on ScanNet [10].** Our method equals to GIORIE-SLAM [75], giving the average lowest trajectory error. Results for the RGB-D methods are from [30]. Note that all methods with a * are concurrent works.

Method	f1/desk	f2/xyz	f3/off	Avg.-3	f1/desk2	f1/room	Avg.-5
<i>RGB-D Input</i>							
SplaTAM [24]	3.4	1.2	5.2	3.3	6.5	11.1	5.5
GS-SLAM* [69]	1.5	1.6	1.7	1.6	-	-	-
GO-SLAM [79]	1.5	0.6	1.3	1.1	-	4.7	-
MonoGS [38]	1.4	1.4	1.5	1.5	5.1	6.3	3.1
<i>RGB Input</i>							
MonoGS [38]	3.8	5.2	2.9	4.0	75.7	76.6	32.8
Photo-SLAM [21]	1.5	1.0	1.3	1.3	-	-	-
DIM-SLAM [28]	2.0	0.6	2.3	1.6	-	-	-
GO-SLAM [79]	1.6	0.6	1.5	1.2	2.8	5.2	2.3
MoD-SLAM* [80]	1.5	0.7	1.1	1.1	-	-	-
Q-SLAM* [46]	1.3	0.9	-	-	2.3	4.9	-
GIORIE-SLAM* [75]	1.6	0.2	1.4	1.1	2.8	4.2	2.1
Ours	1.6	0.2	1.4	1.1	2.8	4.2	2.1

Table S10: **Tracking Accuracy ATE RMSE [cm] ↓ on TUM-RGBD [56].** Our method equals to GIORIE-SLAM [75], giving the average lowest trajectory error. Note that all methods with a * are concurrent works.

B.2 Full Evaluations Data

In tab. S11, tab. S12 and tab. S13, we provide the full per scene results on all commonly reported metrics on Replica [54], TUM-RGBD [56] and ScanNet [10].

The reconstruction results are only measured on Replica since the other two datasets are real world datasets which lack quality ground truth meshes.

		Metric	R-0	R-1	R-2	0-0	0-1	0-2	0-3	0-4	Avg.
Reconstruction		Render Depth L1 ↓	2.90	2.16	2.18	2.44	1.97	2.46	2.62	2.53	2.41
		Accuracy ↓	1.99	1.91	2.06	3.96	2.03	3.45	2.15	1.89	2.43
		Completion ↓	3.78	3.38	3.34	2.75	3.33	4.36	3.96	4.25	3.64
		Comp. Rat. ↑	85.47	86.88	86.12	87.32	85.17	81.37	82.25	82.95	84.69
Rendering	Keyframes	PSNR ↑	32.25	34.31	35.95	40.81	40.64	35.19	35.03	37.40	36.45
		SSIM ↑	0.91	0.93	0.95	0.98	0.97	0.96	0.95	0.98	0.95
		LPIPS ↓	0.10	0.09	0.06	0.05	0.05	0.07	0.06	0.04	0.06
Tracking	Keyframes Trajectory	ATE RMSE ↓	0.29	0.38	0.24	0.27	0.35	0.34	0.42	0.43	0.34
	Full Trajectory	ATE RMSE ↓	0.29	0.33	0.25	0.29	0.35	0.34	0.42	0.43	0.34
Number of Gaussians	1000x		116	116	91	76	66	134	114	106	102

Table S11: **Full Evaluation on Replica [54]**. We show the ATE RMSE [cm] evaluation on the keyframes as well as on the full trajectory.

		Metric	f1/desk	f1/desk2	f1/room	f2/xyz	f3/office	Avg.
Rendering	Keyframes	PSNR ↑	25.61	23.98	24.06	29.53	26.05	25.85
		SSIM ↑	0.84	0.81	0.80	0.90	0.84	0.84
		LPIPS ↓	0.18	0.23	0.24	0.08	0.20	0.19
Depth Rendering	Keyframes	Depth L1 ↓ [cm]	8.05	15.70	15.05	14.53	25.59	15.78
Tracking	Key Frames Trajectory	ATE RMSE ↓	1.92	3.05	4.43	0.23	1.41	2.21
	Full Trajectory	ATE RMSE ↓	1.65	2.79	4.16	0.22	1.44	2.05
Number of Gaussians	1000x		88	78	211	173	114	133

Table S12: **Full Evaluation on TUM-RGBD [56]**.

		Metric	0000	0054	0059	0106	0169	0181	0207	0233	Avg.
Rendering	Keyframes	PSNR ↑	28.68	30.21	27.69	27.70	31.14	31.15	30.49	27.48	29.32
		SSIM ↑	0.83	0.85	0.87	0.86	0.87	0.84	0.84	0.78	0.84
		LPIPS ↓	0.19	0.22	0.15	0.18	0.15	0.23	0.19	0.22	0.19
Depth Rendering	Keyframes	Depth L1 ↓ [cm]	8.24	18.24	13.39	23.5	11.49	18.35	13.78	10.19	11.37
Tracking	Key Frames Trajectory	ATE RMSE ↓	5.66	9.17	9.48	7.03	8.72	8.42	7.47	4.97	7.61
	Full Trajectory	ATE RMSE ↓	5.57	9.50	9.11	7.09	8.26	8.39	7.53	5.17	7.58
Number of Gaussians	1000x		144	157	84	108	52	127	121	191	123

Table S13: **Full Evaluation on ScanNet [10]**.

We show the trajectory accuracy measurement of both keyframes and the full trajectory, which is obtained by first linear interpolation between keyframes and using optical flow to refine. The accuracy of these two trajectories are similar. In the main paper, the data we report is always measured on the full trajectory.

B.3 Influence of Monocular Depth

While we show that the monocular depth improves the geometric estimation capability of our framework, it may still be erroneous. To better understand the accuracy of the monocular depth, we replace it with the ground truth sensor depth instead. This experiment acts as the upper bound of our method if the monocular depth is perfect. The experiments are done on Replica [54] and are shown in tab. S14. Compared with the standard setting with the monocular depth, the ground truth depth setting gives improvements on both reconstruction and rendering quality, which reveals that our method still has potential to achieve better mapping results once better monocular depth is available.

	Metric	R-0	R-1	R-2	0-0	0-1	0-2	0-3	0-4	Avg.
Recon- struction	Render Depth L1 ↓	2.38	1.31	1.73	1.15	1.60	1.29	5.71	1.93	2.14
	Accuracy ↓	1.29	0.91	1.05	1.22	0.83	0.96	1.24	1.07	1.07
	Completion ↓	3.43	2.83	2.66	1.50	2.46	3.57	3.46	3.61	2.94
	Comp. Rat. ↑	86.61	88.69	88.70	93.44	89.09	85.20	84.60	85.32	87.71
Rendering	PSNR ↑	35.66	37.65	38.87	43.95	43.28	37.93	37.41	39.88	39.33
	SSIM ↑	0.96	0.96	0.97	0.99	0.98	0.96	0.96	0.98	0.97
	LPIPS ↓	0.04	0.05	0.03	0.02	0.02	0.06	0.04	0.03	0.04
Tracking	ATE RMSE ↓	0.29	0.38	0.24	0.28	0.39	0.35	0.45	0.40	0.35

Table S14: **Full Evaluations on Replica [54] with ground truth depth.** Both reconstruction and rendering results improve significantly with the ground truth depth, suggesting that our method is bounded by the quality of current day monocular depth estimation. Since we do not require any extra training or fine-tuning of the monocular depth estimator, it is easy to plug in a better estimator once available. Tracking performance does not change much.

Since our method does not require further training or fine-tuning for the monocular depth, it is quite easy to just replace the current off-the-shelf monocular depth estimator with a better one.

B.4 Impact of Deformation

During runtime, we deform the 3D Gaussian map to account for adjustments to poses and depth that have already been integrated into the existing map. An alternative to performing the deformation is to solely rely on optimization to resolve the new map. We conduct two experiments to show the benefit of performing the deformation, especially when it comes to rendering accuracy. In tab. S15, we vary the number of final refinement iterations and evaluate the rendering depth L1 and PSNR on the Replica `office_0` scene. We find that utilizing online 3D Gaussian deformations yields better rendering and depth L1 accuracy regardless of the number of iterations. In tab. S16 we conduct the same experiment, but over a set of scenes on ScanNet. We find that on average, by enabling the deformation, we achieve higher rendering accuracy and lower depth L1 error. The improvement is, however, more significant when it comes to the rendering accuracy.

Nbr of Final Iterations β		Metric	0K	0.5K	1K	2K
Reconstruction	W/O Deform	Render Depth L1 ↓	8.84	3.49	2.64	2.6
	W Deform	Render Depth L1 ↓	6.55	2.37	2.34	2.40
Rendering	W/O Deform	PSNR ↑	22.86	34.30	37.66	37.86
	W Deform	PSNR ↑	30.50	39.87	40.59	41.20

Table S15: **Gaussian Deformation Ablation on Replica [54] `office_0`.**

	Metric	0000	0054	0059	0106	0169	0181	0207	Avg.
Rendering	W/O Deform	PSNR↑	25.15	28.39	27.77	25.25	29.41	30.38	29.30
	W Deform	PSNR↑	28.68	30.21	27.69	27.70	31.14	31.15	30.49
Depth Rendering	W/O Deform	L1↓ [cm]	7.86	22.81	10.51	24.19	11.54	18.48	15.58
	W Deform	L1↓ [cm]	8.24	18.24	13.39	23.5	11.49	18.35	15.28

Table S16: **Gaussian Deformation Ablation on ScanNet [10].**

B.5 Final Refinement Iterations

After the final global BA step, we perform a final refinement, similar to MonoGS[38], but include the geometric depth loss as well and do not only refine with a color loss. We ablate the influence on the results by varying the number of iterations of the final refinement in tab. S17. We find that the rendering accuracy increases monotonically with the number of iterations while the geometric accuracy decreases with more than 2K iterations. We believe this to be a result of fitting to the noisy monocular depth. We choose to use 2K iterations since this provides the best trade-off between rendering and geometric accuracy. 2K iterations takes around 15 seconds on our benchmark hardware which consists of an AMD Ryzen Threadripper Pro 3945WX 12-Cores with an NVIDIA GeForce RTX 3090 Ti with 24 GB of memory.

Nbr of Final Iterations β		Metric	2K	5K	10K	26K
Reconstruction		Render Depth L1 \downarrow	2.36	2.45	2.51	2.59
		Accuracy \downarrow	2.46	2.66	2.84	3.02
		Completion \downarrow	3.60	3.61	3.59	3.60
		Comp. Rat. \uparrow	84.87	84.71	84.80	84.77
Rendering	Keyframes	PSNR \uparrow	36.77	37.80	38.41	38.95

Table S17: **Final Refinement Iterations Ablation on Replica [54]**. The results are averaged over the 8 scenes.

B.6 Impact of Downsampling Factor

During mapping, the point cloud formed from unprojecting the depth input is downsampled to avoid adding redundant Gaussians to the scene representation. We investigate the impact of using stronger versus weaker downsampling in tab. S18 where we also compare to the sensitivity of MonoGS[38] with respect to the same parameter. Tab. S18 shows that both systems are not very sensitive to the model compression as a result of a larger downsampling factor θ . When both systems use the same number of Gaussians on average ($\theta = 32$ for MonoGS and $\theta = 64$ for our method), we find that our method performs significantly better in terms of depth rerendering and photometric accuracy. For all results in the main paper, we use $\theta = 32$.

Downsampling Factor θ		Metric	16	32	64
Reconstruction	Ours	Render Depth L1 \downarrow	2.38	2.40	2.46
	MonoGS [38]		33.43	28.47	28.09
Rendering	Ours	PSNR \uparrow	36.63	36.45	36.31
	MonoGS [38]		31.17	30.87	29.64
Number of Gaussians	Ours	1000x \downarrow	141	102	83
	MonoGS [38]		97	83	73

Table S18: **Downsampling Factor θ Ablation on Replica [54]**. The results are averaged over the 8 scenes.

B.7 Runtime Evaluation

To be consistent with the keyframe selection hyperparameters of MonoGS [38], we report on the same parameters as MonoGS uses by default. In practice, this means that few keyframes from the tracking system (determined via mean optical flow thresholding) are actually filtered out and not mapped. In tab. S19, we show that by altering the hyperparameters, we can speed up the system during runtime, while still rendering and reconstructing the scene well. Note that we evaluate the rendering performance on the same set of views for all runs. We benchmark the runtime on an AMD Ryzen Threadripper Pro 3945WX 12-Cores with an NVIDIA GeForce RTX 3090 Ti with 24 GB of memory. We note that we currently do not leverage multiprocessing to the amount possible in practice *i.e.* currently we first do tracking and then mapping *i.e.* there is no simultaneous tracking and mapping. This is, however, straightforward to include, which should further speed up the runtime.

$k_{f_{cov}}, k_{f_m}$		0.95, 0.04	0.90, 0.08	0.85, 0.08	0.80, 0.12	0.70, 0.16	0.60, 0.20	0.50, 0.30
Reconstruction	Render Depth L1 \downarrow	2.90	2.94	2.97	3.08	3.37	3.53	4.78
	Accuracy \downarrow	1.99	1.94	2.06	2.04	2.54	3.20	6.20
	Completion \downarrow	3.78	3.76	3.79	3.77	3.86	3.93	5.23
	Comp. Rat. \uparrow	85.47	85.58	85.39	85.53	85.03	84.33	80.38
Rendering	PSNR \uparrow	32.25	31.65	31.31	30.59	30.12	29.25	27.59
Runtime	FPS \uparrow	1.24	1.45	1.62	2.02	2.50	3.03	3.67

Table S19: **Keyframe Hyperparameter Search on Replica [54] room 0**. By changing the keyframe selection hyperparameters, we can speed up our runtime without impacting reconstruction and rendering too much. We evaluate the rendering performance on the same set of frames for all runs. In comparison, with the default $k_{f_{cov}} = 0.95$, $k_{f_m} = 0.04$, MonoGS [38] yields PSNR: 26.12 and render depth L1: 17.38 cm.

B.8 Additional Qualitative Reconstructions

In fig. S6 we show additional qualitative results from the Replica dataset on normal shaded meshes.

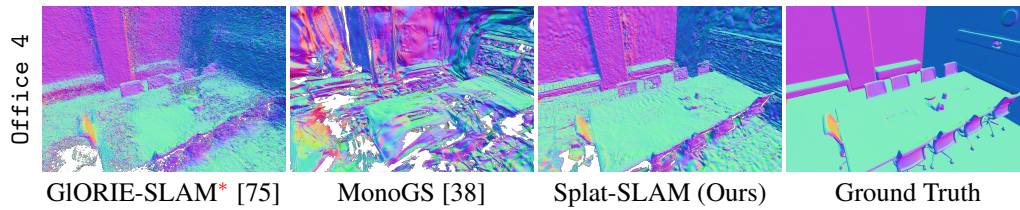


Figure S6: **Reconstruction Results on Replica [54]**. Our method improves upon the geometric accuracy compared to existing works, when observing the normal shaded meshes. In particular, GIORIE-SLAM suffers from floating point artifacts. MonoGS suffers badly from a lack of proxy depth, despite multiview optimization.

References

- [1] Azinović, D., Martin-Brualla, R., Goldman, D.B., Nießner, M., Thies, J.: Neural rgb-d surface reconstruction. In: IEEE/CVF Conference on Computer Vision and Pattern Recognition. pp. 6290–6301 (2022)
- [2] Bosse, M., Newman, P., Leonard, J., Soika, M., Feiten, W., Teller, S.: An atlas framework for scalable mapping. In: 2003 IEEE International Conference on Robotics and Automation (Cat. No. 03CH37422). vol. 2, pp. 1899–1906. IEEE (2003)
- [3] Božič, A., Palafox, P., Thies, J., Dai, A., Nießner, M.: Transformerfusion: Monocular rgb scene reconstruction using transformers. arXiv preprint arXiv:2107.02191 (2021)
- [4] Cao, Y.P., Kobbelt, L., Hu, S.M.: Real-time high-accuracy three-dimensional reconstruction with consumer rgb-d cameras. *ACM Transactions on Graphics (TOG)* **37**(5), 1–16 (2018)
- [5] Chen, J., Bautembach, D., Izadi, S.: Scalable real-time volumetric surface reconstruction. *ACM Transactions on Graphics (ToG)* **32**(4), 1–16 (2013)
- [6] Cho, H.M., Jo, H., Kim, E.: Sp-slam: Surfel-point simultaneous localization and mapping. *IEEE/ASME Transactions on Mechatronics* **27**(5), 2568–2579 (2021)
- [7] Choi, S., Zhou, Q.Y., Koltun, V.: Robust reconstruction of indoor scenes. In: IEEE Conference on Computer Vision and Pattern Recognition. pp. 5556–5565 (2015)
- [8] Chung, C.M., Tseng, Y.C., Hsu, Y.C., Shi, X.Q., Hua, Y.H., Yeh, J.F., Chen, W.C., Chen, Y.T., Hsu, W.H.: Orbeez-slam: A real-time monocular visual slam with orb features and nerf-realized mapping. arXiv preprint arXiv:2209.13274 (2022)
- [9] Curless, B., Levoy, M.: Volumetric method for building complex models from range images. In: SIGGRAPH Conference on Computer Graphics. ACM (1996)
- [10] Dai, A., Chang, A.X., Savva, M., Halber, M., Funkhouser, T., Nießner, M.: ScanNet: Richly-annotated 3D reconstructions of indoor scenes. In: Conference on Computer Vision and Pattern Recognition (CVPR). IEEE/CVF (2017). <https://doi.org/10.1109/CVPR.2017.261>, <http://arxiv.org/abs/1702.04405>
- [11] Dai, A., Nießner, M., Zollhöfer, M., Izadi, S., Theobalt, C.: Bundlerefusion: Real-time globally consistent 3d reconstruction using on-the-fly surface reintegration. *ACM Transactions on Graphics (ToG)* **36**(4), 1 (2017)
- [12] Eftekhari, A., Sax, A., Malik, J., Zamir, A.: Omnidata: A scalable pipeline for making multi-task mid-level vision datasets from 3d scans. In: Proceedings of the IEEE/CVF International Conference on Computer Vision. pp. 10786–10796 (2021)
- [13] Endres, F., Hess, J., Engelhard, N., Sturm, J., Cremers, D., Burgard, W.: An evaluation of the rgb-d slam system. In: 2012 IEEE international conference on robotics and automation. pp. 1691–1696. IEEE (2012)
- [14] Engel, J., Schöps, T., Cremers, D.: Lsd-slam: Large-scale direct monocular slam. In: European conference on computer vision. pp. 834–849. Springer (2014)
- [15] Fioraio, N., Taylor, J., Fitzgibbon, A., Di Stefano, L., Izadi, S.: Large-scale and drift-free surface reconstruction using online subvolume registration. In: Proceedings of the IEEE Conference on Computer Vision and Pattern Recognition. pp. 4475–4483 (2015)
- [16] Henry, P., Fox, D., Bhowmik, A., Mongia, R.: Patch volumes: Segmentation-based consistent mapping with rgb-d cameras. In: 2013 International Conference on 3D Vision-3DV 2013. pp. 398–405. IEEE (2013)
- [17] Henry, P., Krainin, M., Herbst, E., Ren, X., Fox, D.: Rgb-d mapping: Using kinect-style depth cameras for dense 3d modeling of indoor environments. *The international journal of Robotics Research* **31**(5), 647–663 (2012)
- [18] Hu, J., Mao, M., Bao, H., Zhang, G., Cui, Z.: CP-SLAM: Collaborative neural point-based SLAM system. In: Thirty-seventh Conference on Neural Information Processing Systems (2023), <https://openreview.net/forum?id=dFSzZm6dTC>
- [19] Hua, T., Bai, H., Cao, Z., Liu, M., Tao, D., Wang, L.: Hi-map: Hierarchical factorized radiance field for high-fidelity monocular dense mapping. arXiv preprint arXiv:2401.03203 (2024)
- [20] Hua, T., Bai, H., Cao, Z., Wang, L.: Fmapping: Factorized efficient neural field mapping for real-time dense rgb slam. arXiv preprint arXiv:2306.00579 (2023)

- [21] Huang, H., Li, L., Cheng, H., Yeung, S.K.: Photo-slam: Real-time simultaneous localization and photorealistic mapping for monocular, stereo, and rgb-d cameras. arXiv preprint arXiv:2311.16728 (2023)
- [22] Kähler, O., Prisacariu, V.A., Murray, D.W.: Real-time large-scale dense 3d reconstruction with loop closure. In: Computer Vision—ECCV 2016: 14th European Conference, Amsterdam, The Netherlands, October 11–14, 2016, Proceedings, Part VIII 14. pp. 500–516. Springer (2016)
- [23] Kähler, O., Prisacariu, V.A., Ren, C.Y., Sun, X., Torr, P.H.S., Murray, D.W.: Very high frame rate volumetric integration of depth images on mobile devices. *IEEE Trans. Vis. Comput. Graph.* **21**(11), 1241–1250 (2015). <https://doi.org/10.1109/TVCG.2015.2459891>, <https://doi.org/10.1109/TVCG.2015.2459891>
- [24] Keetha, N., Karhade, J., Jatavallabhula, K.M., Yang, G., Scherer, S., Ramanan, D., Luiten, J.: Splatam: Splat, track and map 3d gaussians for dense rgb-d slam. arXiv preprint (2023)
- [25] Keller, M., Lefloch, D., Lambers, M., Izadi, S., Weyrich, T., Kolb, A.: Real-time 3d reconstruction in dynamic scenes using point-based fusion. In: International Conference on 3D Vision (3DV). pp. 1–8. IEEE (2013)
- [26] Kerbl, B., Kopanas, G., Leimkühler, T., Drettakis, G.: 3d gaussian splatting for real-time radiance field rendering. *ACM Transactions on Graphics* **42**(4) (2023)
- [27] Kerl, C., Sturm, J., Cremers, D.: Dense visual slam for rgb-d cameras. In: 2013 IEEE/RSJ International Conference on Intelligent Robots and Systems. pp. 2100–2106. IEEE (2013)
- [28] Li, H., Gu, X., Yuan, W., Yang, L., Dong, Z., Tan, P.: Dense rgb slam with neural implicit maps. In: Proceedings of the International Conference on Learning Representations (2023), <https://openreview.net/forum?id=QUK1Ex1bba>
- [29] Li, K., Tang, Y., Prisacariu, V.A., Torr, P.H.: Biv-fusion: Dense 3d reconstruction using bi-level neural volume fusion. In: IEEE/CVF Conference on Computer Vision and Pattern Recognition. pp. 6166–6175 (2022)
- [30] Liso, L., Sandström, E., Yugay, V., Van Gool, L., Oswald, M.R.: Loopy-slam: Dense neural slam with loop closures. arXiv preprint arXiv:2402.09944 (2024)
- [31] Liu, L., Gu, J., Zaw Lin, K., Chua, T.S., Theobalt, C.: Neural sparse voxel fields. *Advances in Neural Information Processing Systems* **33**, 15651–15663 (2020)
- [32] Lorensen, W.E., Cline, H.E.: Marching cubes: A high resolution 3d surface construction algorithm. *ACM siggraph computer graphics* **21**(4), 163–169 (1987)
- [33] Mahdi Johari, M., Carta, C., Fleuret, F.: Eslam: Efficient dense slam system based on hybrid representation of signed distance fields. arXiv e-prints pp. arXiv–2211 (2022)
- [34] Maier, R., Schaller, R., Cremers, D.: Efficient online surface correction for real-time large-scale 3d reconstruction. arXiv 2017. arXiv preprint arXiv:1709.03763 (2017)
- [35] Maier, R., Sturm, J., Cremers, D.: Submap-based bundle adjustment for 3d reconstruction from rgb-d data. In: Pattern Recognition: 36th German Conference, GCPR 2014, Münster, Germany, September 2–5, 2014, Proceedings 36. pp. 54–65. Springer (2014)
- [36] Mao, Y., Yu, X., Wang, K., Wang, Y., Xiong, R., Liao, Y.: Ngel-slam: Neural implicit representation-based global consistent low-latency slam system. arXiv preprint arXiv:2311.09525 (2023)
- [37] Marniok, N., Johannsen, O., Goldluecke, B.: An efficient octree design for local variational range image fusion. In: German Conference on Pattern Recognition (GCPR). pp. 401–412. Springer (2017)
- [38] Matsuki, H., Murai, R., Kelly, P.H., Davison, A.J.: Gaussian splatting slam. arXiv preprint arXiv:2312.06741 (2023)
- [39] Matsuki, H., Sucar, E., Laidow, T., Wada, K., Scona, R., Davison, A.J.: imode: Real-time incremental monocular dense mapping using neural field. In: 2023 IEEE International Conference on Robotics and Automation (ICRA). pp. 4171–4177. IEEE (2023)
- [40] Matsuki, H., Tateno, K., Niemyer, M., Tombari, F.: Newton: Neural view-centric mapping for on-the-fly large-scale slam. arXiv preprint arXiv:2303.13654 (2023)
- [41] Naumann, J., Xu, B., Leutenegger, S., Zuo, X.: Nerf-vo: Real-time sparse visual odometry with neural radiance fields. arXiv preprint arXiv:2312.13471 (2023)

- [42] Newcombe, R.A., Izadi, S., Hilliges, O., Molyneaux, D., Kim, D., Davison, A.J., Kohli, P., Shotton, J., Hodges, S., Fitzgibbon, A.W.: Kinectfusion: Real-time dense surface mapping and tracking. In: ISMAR. vol. 11, pp. 127–136 (2011)
- [43] Nießner, M., Zollhöfer, M., Izadi, S., Stamminger, M.: Real-time 3d reconstruction at scale using voxel hashing. *ACM Transactions on Graphics (TOG)* **32** (11 2013). <https://doi.org/10.1145/2508363.2508374>
- [44] Oleynikova, H., Taylor, Z., Fehr, M., Siegart, R., Nieto, J.I.: Voxblox: Incremental 3d euclidean signed distance fields for on-board MAV planning. In: 2017 IEEE/RSJ International Conference on Intelligent Robots and Systems, IROS 2017, Vancouver, BC, Canada, September 24–28, 2017. pp. 1366–1373. IEEE (2017). <https://doi.org/10.1109/IROS.2017.8202315>, <https://doi.org/10.1109/IROS.2017.8202315>
- [45] Ortiz, J., Clegg, A., Dong, J., Sucar, E., Novotny, D., Zollhoefer, M., Mukadam, M.: isdf: Real-time neural signed distance fields for robot perception. *arXiv preprint arXiv:2204.02296* (2022)
- [46] Peng, C., Xu, C., Wang, Y., Ding, M., Yang, H., Tomizuka, M., Keutzer, K., Pavone, M., Zhan, W.: Q-slam: Quadric representations for monocular slam. *arXiv preprint arXiv:2403.08125* (2024)
- [47] Peng, S., Niemeyer, M., Mescheder, L., Pollefeys, M., Geiger, A.: Convolutional Occupancy Networks. In: European Conference Computer Vision (ECCV). CVF (2020), <https://www.microsoft.com/en-us/research/publication/convolutional-occupancy-networks/>
- [48] Reijgwart, V., Millane, A., Oleynikova, H., Siegart, R., Cadena, C., Nieto, J.: Voxgraph: Globally consistent, volumetric mapping using signed distance function submaps. *IEEE Robotics and Automation Letters* **5**(1), 227–234 (2019)
- [49] Rosinol, A., Leonard, J.J., Carlone, L.: NeRF-SLAM: Real-Time Dense Monocular SLAM with Neural Radiance Fields. *arXiv* (2022), <http://arxiv.org/abs/2210.13641>
- [50] Sandström, E., Li, Y., Van Gool, L., Oswald, M.R.: Point-slam: Dense neural point cloud-based slam. In: International Conference on Computer Vision (ICCV). IEEE/CVF (2023)
- [51] Sandström, E., Ta, K., Gool, L.V., Oswald, M.R.: Uncle-SLAM: Uncertainty learning for dense neural SLAM. In: International Conference on Computer Vision Workshops (ICCVW) (2023)
- [52] Schops, T., Sattler, T., Pollefeys, M.: BAD SLAM: Bundle adjusted direct RGB-D SLAM. In: CVF/IEEE Conference on Computer Vision and Pattern Recognition (CVPR) (2019)
- [53] Steinbrucker, F., Kerl, C., Cremers, D.: Large-scale multi-resolution surface reconstruction from rgb-d sequences. In: IEEE International Conference on Computer Vision. pp. 3264–3271 (2013)
- [54] Straub, J., Whelan, T., Ma, L., Chen, Y., Wijmans, E., Green, S., Engel, J.J., Mur-Artal, R., Ren, C., Verma, S., et al.: The replica dataset: A digital replica of indoor spaces. *arXiv preprint arXiv:1906.05797* (2019)
- [55] Stückler, J., Behnke, S.: Multi-resolution surfel maps for efficient dense 3d modeling and tracking. *Journal of Visual Communication and Image Representation* **25**(1), 137–147 (2014)
- [56] Sturm, J., Engelhard, N., Endres, F., Burgard, W., Cremers, D.: A benchmark for the evaluation of RGB-D SLAM systems. In: International Conference on Intelligent Robots and Systems (IROS). IEEE/RSJ (2012). <https://doi.org/10.1109/IROS.2012.6385773>, <http://ieeexplore.ieee.org/document/6385773/>
- [57] Sucar, E., Liu, S., Ortiz, J., Davison, A.J.: iMAP: Implicit Mapping and Positioning in Real-Time. In: International Conference on Computer Vision (ICCV). IEEE/CVF (2021). <https://doi.org/10.1109/ICCV48922.2021.00617>, <https://ieeexplore.ieee.org/document/9710431/>
- [58] Sun, J., Xie, Y., Chen, L., Zhou, X., Bao, H.: Neuralrecon: Real-time coherent 3d reconstruction from monocular video. In: IEEE/CVF Conference on Computer Vision and Pattern Recognition. pp. 15598–15607 (2021)
- [59] Tang, Y., Zhang, J., Yu, Z., Wang, H., Xu, K.: Mips-fusion: Multi-implicit-submaps for scalable and robust online neural rgb-d reconstruction. *arXiv preprint arXiv:2308.08741* (2023)
- [60] Teed, Z., Deng, J.: Raft: Recurrent all-pairs field transforms for optical flow. In: Computer Vision–ECCV 2020: 16th European Conference, Glasgow, UK, August 23–28, 2020, Proceedings, Part II 16. pp. 402–419. Springer (2020)

- [61] Teed, Z., Deng, J.: Droid-slam: Deep visual slam for monocular, stereo, and rgb-d cameras. *Advances in neural information processing systems* **34**, 16558–16569 (2021)
- [62] Tosi, F., Zhang, Y., Gong, Z., Sandström, E., Mattoccia, S., Oswald, M.R., Poggi, M.: How nerfs and 3d gaussian splatting are reshaping slam: a survey (2024)
- [63] Wang, H., Wang, J., Liang, W.: Online reconstruction of indoor scenes from rgb-d streams. In: *Proceedings of the IEEE Conference on Computer Vision and Pattern Recognition*. pp. 3271–3279 (2016)
- [64] Wang, H., Wang, J., Agapito, L.: Co-slam: Joint coordinate and sparse parametric encodings for neural real-time slam. In: *Proceedings of the IEEE/CVF Conference on Computer Vision and Pattern Recognition (CVPR)*. pp. 13293–13302 (June 2023)
- [65] Wang, Z., Bovik, A.C., Sheikh, H.R., Simoncelli, E.P.: Image quality assessment: from error visibility to structural similarity. *IEEE transactions on image processing* **13**(4), 600–612 (2004)
- [66] Weder, S., Schonberger, J., Pollefeys, M., Oswald, M.R.: Routedfusion: Learning real-time depth map fusion. In: *IEEE/CVF Conference on Computer Vision and Pattern Recognition*. pp. 4887–4897 (2020)
- [67] Weder, S., Schonberger, J.L., Pollefeys, M., Oswald, M.R.: Neurfusion: Online depth fusion in latent space. In: *IEEE/CVF Conference on Computer Vision and Pattern Recognition*. pp. 3162–3172 (2021)
- [68] Whelan, T., Leutenegger, S., Salas-Moreno, R., Glocker, B., Davison, A.: Elasticfusion: Dense slam without a pose graph. In: *Robotics: Science and Systems (RSS)* (2015)
- [69] Yan, C., Qu, D., Wang, D., Xu, D., Wang, Z., Zhao, B., Li, X.: Gs-slam: Dense visual slam with 3d gaussian splatting. *arXiv preprint arXiv:2311.11700* (2023)
- [70] Yan, Z., Ye, M., Ren, L.: Dense visual slam with probabilistic surfel map. *IEEE transactions on visualization and computer graphics* **23**(11), 2389–2398 (2017)
- [71] Yang, L., Kang, B., Huang, Z., Xu, X., Feng, J., Zhao, H.: Depth anything: Unleashing the power of large-scale unlabeled data. *arXiv preprint arXiv:2401.10891* (2024)
- [72] Yang, X., Li, H., Zhai, H., Ming, Y., Liu, Y., Zhang, G.: Vox-fusion: Dense tracking and mapping with voxel-based neural implicit representation. In: *IEEE International Symposium on Mixed and Augmented Reality (ISMAR)*. pp. 499–507. IEEE (2022)
- [73] Yang, X., Ming, Y., Cui, Z., Calway, A.: Fd-slam: 3-d reconstruction using features and dense matching. In: *2022 International Conference on Robotics and Automation (ICRA)*. pp. 8040–8046. IEEE (2022)
- [74] Yugay, V., Li, Y., Gevers, T., Oswald, M.R.: Gaussian-slam: Photo-realistic dense slam with gaussian splatting (2023)
- [75] Zhang, G., Sandström, E., Zhang, Y., Patel, M., Van Gool, L., Oswald, M.R.: Glorie-slam: Globally optimized rgb-only implicit encoding point cloud slam. *arXiv preprint arXiv:2403.19549* (2024)
- [76] Zhang, H., Chen, G., Wang, Z., Wang, Z., Sun, L.: Dense 3d mapping for indoor environment based on feature-point slam method. In: *2020 the 4th International Conference on Innovation in Artificial Intelligence*. pp. 42–46 (2020)
- [77] Zhang, R., Isola, P., Efros, A.A., Shechtman, E., Wang, O.: The unreasonable effectiveness of deep features as a perceptual metric. In: *IEEE conference on computer vision and pattern recognition*. pp. 586–595 (2018)
- [78] Zhang, W., Sun, T., Wang, S., Cheng, Q., Haala, N.: Hi-slam: Monocular real-time dense mapping with hybrid implicit fields. *IEEE Robotics and Automation Letters* (2023)
- [79] Zhang, Y., Tosi, F., Mattoccia, S., Poggi, M.: Go-slam: Global optimization for consistent 3d instant reconstruction. In: *Proceedings of the IEEE/CVF International Conference on Computer Vision*. pp. 3727–3737 (2023)
- [80] Zhou, H., Guo, Z., Liu, S., Zhang, L., Wang, Q., Ren, Y., Li, M.: Mod-slam: Monocular dense mapping for unbounded 3d scene reconstruction (2024)
- [81] Zhu, Z., Peng, S., Larsson, V., Cui, Z., Oswald, M.R., Geiger, A., Pollefeys, M.: Nicer-slam: Neural implicit scene encoding for rgb slam. *arXiv preprint arXiv:2302.03594* (2023)

- [82] Zhu, Z., Peng, S., Larsson, V., Xu, W., Bao, H., Cui, Z., Oswald, M.R., Pollefeys, M.: Nice-slam: Neural implicit scalable encoding for slam. In: IEEE/CVF Conference on Computer Vision and Pattern Recognition. pp. 12786–12796 (2022)
- [83] Zou, Z.X., Huang, S.S., Cao, Y.P., Mu, T.J., Shan, Y., Fu, H.: Mononeuralfusion: Online monocular neural 3d reconstruction with geometric priors. arXiv preprint arXiv:2209.15153 (2022)
- [84] Zwicker, M., Pfister, H., Van Baar, J., Gross, M.: Surface splatting. In: Proceedings of the 28th annual conference on Computer graphics and interactive techniques. pp. 371–378 (2001)